Nanoscale super-resolution imaging via a metal–dielectric metamaterial lens system

2011 J. Phys. D: Appl. Phys. 44 415101

(http://iopscience.iop.org/0022-3727/44/41/415101)

J. Phys. D: Appl. Phys. **44** (2011) 415101 (7pp) doi:10.1088/0022-3727/44/41/415101

Nanoscale super-resolution imaging via a metal–dielectric metamaterial lens system

Yanhui Zhao, Ahmad Ahsan Nawaz, Sz-Chin Steven Lin, Qingzhen Hao, Brian Kiraly and Tony Jun Huang

Department of Engineering Science and Mechanics, The Pennsylvania State University, University Park, PA 16802, USA

E-mail: junhuang@psu.edu

Received 28 February 2011, in final form 4 August 2011
Published 26 September 2011
Online at stacks.iop.org/JPhysD/44/415101

Abstract
We have proposed a method for super-resolution imaging using an interlayer cascaded structure comprising two metamaterial lenses. The metamaterial lenses are designed using the effective medium theory. The lens structures consist of two different planar dielectric films alternated with similar thin metallic films, making a diverging and converging lens. With this two-lens system, an image is formed at the output surface of the lens with subwavelength resolution. We have shown, through numerical simulations and an analytical approach, that an image with resolution nine times smaller than the light wavelength (365 nm) is achievable with this metamaterial lens system. The loss during transmission through the lens system is smaller compared with the hyperlens configuration with a similar design.

(Some figures in this article are in colour only in the electronic version)

In optics, diffraction limit has always been an obstacle that prevents many optical components from being integrated within micro/nanosystems [1]. Super-resolution imaging can provide a method to circumvent this limit and has been a prominent research focus in optics since Pendry proposed the idea of a perfect lens in 2002 [2]. By introducing a material with a negative refractive index, all the Fourier components, including the propagating and evanescent waves, can be transmitted through such a material, yielding prefect images without resolution limitations and aberration. Although exciting, the realization of a material with negative refractive index poses formidable challenges with current fabrication techniques. Feasible solutions have been reported using quasi-static approximations of electromagnetic field, which deal with permittivity and permeability separately at the nanoscale [3–8]. Compared with perfect imaging, super-resolution imaging is easier to obtain because the fabrication requirements are less stringent. It has been established that super-resolution imaging is possible in materials with negative dielectric permittivity, due to the decoupling of the electric and magnetic fields in the static approximation [9–14]. This simplified perfect lens, called a superlens, has been extensively investigated because of its relatively simple fabrication and practical application. Another way to achieve perfect/super-resolution imaging is to use metamaterials designed by transformation optics [15, 16] or conformal mapping [17]; these methods have been applied to design many novel optical devices such as optical cloaks [18–22], energy harvesters [23, 24], energy concentrators [25, 26] and phase transformers [27]. The optical hyperlens consisting of a multilayer metamaterial demonstrated imaging resolution beyond the diffraction limit [28–30]. A two-dimensional imaging system based on a multilayer metamaterial structure has also been reported [31]. Both superlens and hyperlens rely on the almost perfect matching condition built upon a permittivity match between the metal and the dielectric used. Highly dispersive real metals will cause these designs to be valid only for a small range of frequencies. One viable solution to this dilemma is to use different thicknesses to compensate for the permittivity difference between two different materials [32], and is further extended to use a wire medium to obtain super-resolution imaging without the limitation of material choice [33–35]. Optical bilayers, reported by Smith and co-workers, open another door for imaging beyond diffraction limits by collecting and transmitting evanescent waves through a lens-like structure. Unfortunately, difficulties in realizing two layers without definite permittivity or permeability restrict the application of such an imaging system [36].

In this paper, we have demonstrated super-resolution imaging in an optical multilayer imaging system using an

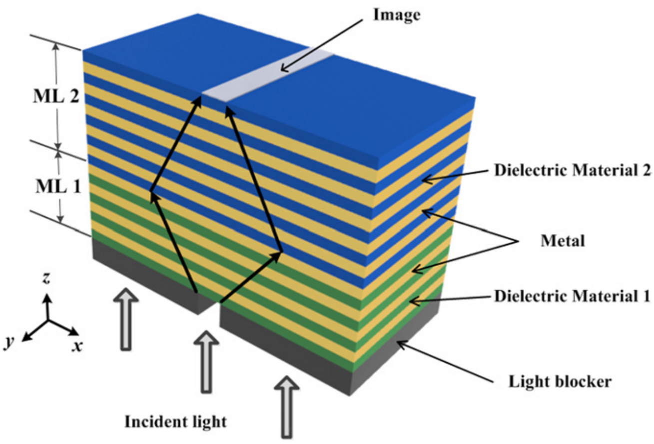

Figure 1. Schematic of the metamaterial lens system for imaging. Incident light passing through the slit object will diverge in metamaterial lens 1 (ML1) and converge in metamaterial lens 2 (ML2), forming an image on the top surface of ML2.

interlayered structure of two different metamaterials. By introducing a metamaterial into the design of the bilayer system, we have shown that super-resolution can be achieved through simple structures with satisfied transmission loss. The initial design of the metamaterial lens was accomplished using the effective medium theory (EMT) [37]. Our design was further confirmed with simulation results conducted with the commercial software COMSOL Multiphysics [38]. Finally, the designed structure was optimized by applying the transfer matrix method (TMM) [39, 40]. The realization of the proposed metamaterial lens system could find applications in areas such as nanolithography/nanoimaging [41], optical storage, sensing [42], plasmonic manipulation [43] and optical modulation [44, 45].

The schematic of the proposed metamaterial lens system is shown in figure 1, which gives details about the imaging process and construction of the metamaterial lenses. The design involves two groups of interlayered structures. Alternate layers of dielectric material 1 (green) and a thin metal film (yellow) form lens 1, while alternate layers of a different dielectric material 2 (blue) and a similar thin metal film (yellow) form lens 2. These two lenses constitute the diverging and the converging parts of the lens structure, respectively. These converging and diverging components allow object near the bottom of the structure to be imaged with resolution well below the diffraction limit.

The physical origin of the imaging effect arises from the unique optical properties of the two metamaterials, which are both comprised of anisotropic metallodielectric interlayered film structures. The performance of the two lenses is determined by parameters such as material properties, thickness of the films/layers and the arrangement of the films. The behaviour of these layered arrangements can be understood with EMT. As the thickness of each layer is less than one-tenth of the incident wavelength, the approximation made by EMT is accurate. According to the EMT approximation, the effective permittivity of the structure can then be related as

$$\begin{aligned} \varepsilon_x &= \varepsilon_y = \varepsilon_{\rm d} f + \varepsilon_{\rm m}(1-f) \\ \varepsilon_z^{-1} &= \varepsilon_{\rm d}^{-1} f + \varepsilon_{\rm m}^{-1}(1-f) \end{aligned} \tag{1}$$

where $\varepsilon_{\rm d}$ denotes the permittivity of dielectrics, $\varepsilon_{\rm m}$ represents the permittivity of the metal materials, f is the filling factor of the dielectric layers, and ε_x and ε_z are the effective permittivities along the transverse and normal directions, respectively. An appropriate filling factor yields combinations of ε_x and ε_z with opposite signs, implying hyperbolic forms of the dispersion relation for transverse magnetic (TM) polarized plane waves. Considering the symmetric relation of the film in the x and y directions, the problem can be simplified using a 2D approach by which the dispersion relation can be expressed as follows [46]:

$$\frac{k_x^2}{\varepsilon_z} + \frac{k_z^2}{\varepsilon_x} = \left(\frac{\omega}{c}\right)^2 \tag{2}$$

where ω is the frequency, $c$is the velocity of light in vacuum, and k_x and k_z represent the wave vectors in the transverse and normal directions, respectively. Two different combinations, $\varepsilon_x < 0, \varepsilon_z > 0$ and $\varepsilon_x > 0, \varepsilon_z < 0$ lead to different hyperbolic dispersion curves, which can be differentiated by checking the locations of their main axis. An illustration of the two hyperbolic dispersion curves is given in figure 2(a).

The group velocity $v_{\rm g} = \nabla_k \omega(k)$ denotes the energy flow direction: normal to the dispersion curves of constant frequency [47, 48]. To further elucidate the direction of Poynting vector, arrows are drawn on the dispersion curves in figure 2(a) indicating its direction [48]. To distinguish between the two lens structures, the corresponding metallodielectric film structures are referred to as metamaterial lens 1 (ML1) and metamaterial lens 2 (ML2). For both lenses, the directional light propagation in the lens is caused by the asymptotic behaviour of the hyperbolic dispersion function. As k_x becomes large, the light propagation direction can be defined by θ with respect to the normal direction

$$\tan\theta = \sqrt{-\frac{\varepsilon_x}{\varepsilon_z}}. \tag{3}$$

The dispersion curves also indicate that the waves with large transversal wave vector ($k_x \geqslant k_0$), which are commonly evanescent waves in natural optical materials, can be transmitted.

We studied this system with an object near the bottom of the structure under normally incident light (z-direction). The light, after being scattered by the object, enters ML1 and diverges mainly along two symmetrical directions determined by equation (3). At the interface of ML1 and ML2, the direction of light propagation will be bent inwards; the extent to which the light is bent is determined by the energy flow direction normal to the intrinsic dispersion curves of ML2, shown as red arrows in figure 2(a). This leads to the reconstruction of the image at the top surface of ML2, provided that the thickness d_1 of ML1 and that of ML2 d_2 roughly satisfy the following relation:

$$\frac{d_1}{d_2} = \frac{\cot(\theta_1)}{\cot(\theta_2)} \tag{4}$$

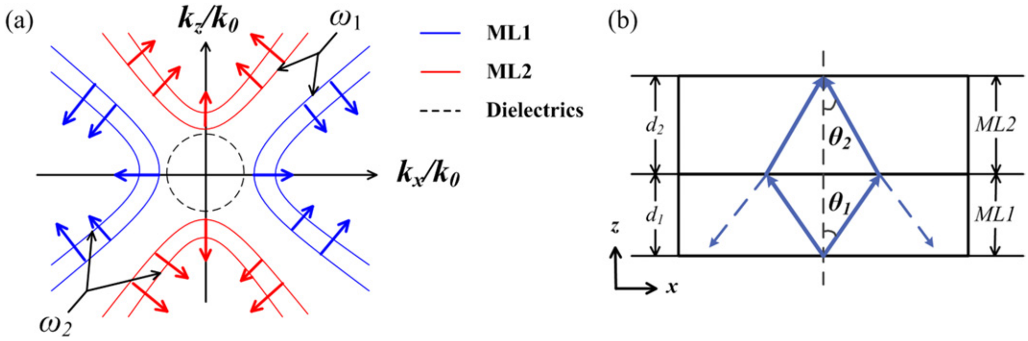

Figure 2. (*a*) Hyperbolic dispersion relations for $\varepsilon_x < 0$, $\varepsilon_z > 0$ (blue) and $\varepsilon_x > 0$, $\varepsilon_z < 0$ (red). The arrows indicate the direction of group velocity for two frequencies with $w_1 < w_2$. The dashed circle represents the dispersion curve for isotropic materials. (*b*) Schematic of imaging process by ML1 ($\varepsilon_x < 0$ and $\varepsilon_z > 0$, below) and ML2 ($\varepsilon_x > 0$ and $\varepsilon_z < 0$, above).

with θ_1 and θ_2 obtained from equation (3). As illustrated above, the object plane and image plane of the interlayered imaging structure are at the top and bottom of the structure, respectively. The working distance in this structure is determined by the total thickness of ML1 and ML2, which can be simply estimated as $d_1 + d_2$.

During the design process, we set the filling factor f for both MLs to be 0.5, making the dielectric and metal films of equal thickness. Such an assumption restricts the permittivity of the metal to be larger than that of the dielectric material in ML1 and smaller for ML2. Given the relation $n^2 = \varepsilon\mu$, where the refractive index is given by n, permittivity by ε and permeability by μ, there is a limited choice of contrast between low and high refractive index dielectric materials. Moreover, the choice of metal (i.e. silver) as the interlayer is limited by its permittivity at the desired frequency, chosen for its popular use in applications such as nanofabrication. For the sake of simplicity, we have chosen the same metal for both ML1 and ML2.

The simulation is conducted using the commercial software COMSOL Mutiphysics. We use silver with a permittivity of $-2.6 + 0.13i$ at 365 nm as an ideal candidate for the metal interlayer in both lenses [49]. The permittivities of the dielectric materials in ML1 and ML2 are selected as 1.0 and 4.84, respectively, corresponding to air and a polymer with a high refractive index. A chromium layer is used at the input surface to block all unwanted incident light, while a slit through the layer acts as an object for imaging. Chromium also has a permittivity of $-10 + 10.8i$, and strongly damps the unwanted propagating surface plasmons excited at its interface with ML1. A chromium layer of 50 nm thickness is sufficient to provide the aforementioned features. The thickness of each alternating metal and dielectric layer is set to 5 nm initially to demonstrate imaging and is optimized later. The calculated effective permittivities are $\varepsilon_x = -0.80$ and $\varepsilon_z = 3.24$ for ML1 and $\varepsilon_x = 1.11$ and $\varepsilon_z = -11.27$ for ML2, corresponding to propagation directions with $\tan\theta_1 = 0.49$ and $\tan\theta_2 = 0.31$ according to equation (3). The relation connecting the total thickness of ML1 and ML2 can be found in equation (4), with known values of θ_1 and θ_2. Here, we set the thickness for ML1 to be 70 nm and that for ML2 to be 130 nm, which approximately meets the criterion of equation (4). The object is a slit of width 20 nm. The incident

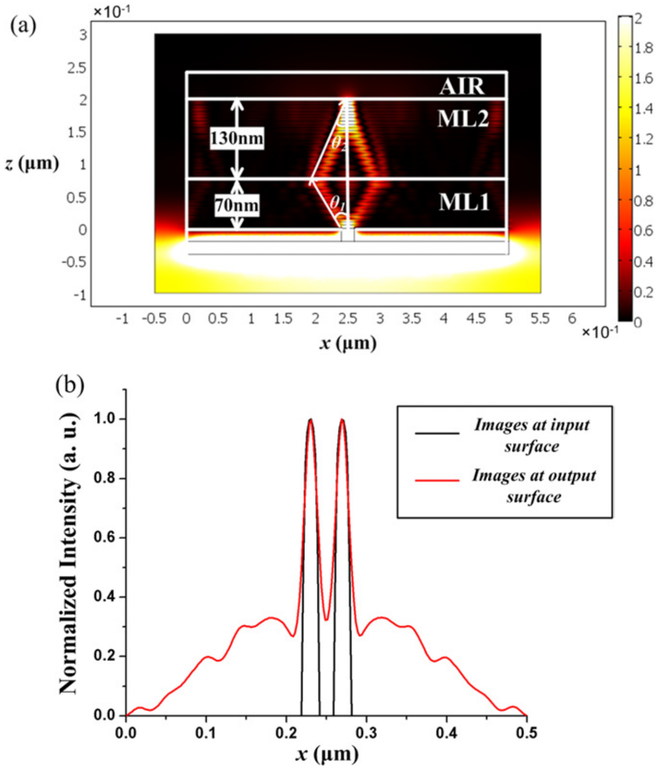

Figure 3. (*a*) Simulation result of ML imaging, corresponding to the structure shown in figure 1. (*b*) Normalized intensity of the images of two slit objects on the input and output planes. Two slit objects are 20 nm in width each and their centre-to-centre distance is 40 nm.

light takes the form of a plane wave impinging normal to the chromium layer as shown by the arrows in figure 1. The simulation is conducted based on the finite element method, where sufficient meshes are needed to ensure a convergent result. The simulation area of 600 nm × 400 nm is divided into approximately 200 000 meshes, determined by the smallest film thickness of 5 nm. Continuous boundary conditions are applied to the inside structure of the imaging system, while a perfect electric conductor condition is used for the outside boundaries enclosing the simulated area. Perfect magnetic conductor conditions are used at the interface of the chromium layer and ML1 to further filter the disturbance caused by both surface plasmons and scattered light. The simulation

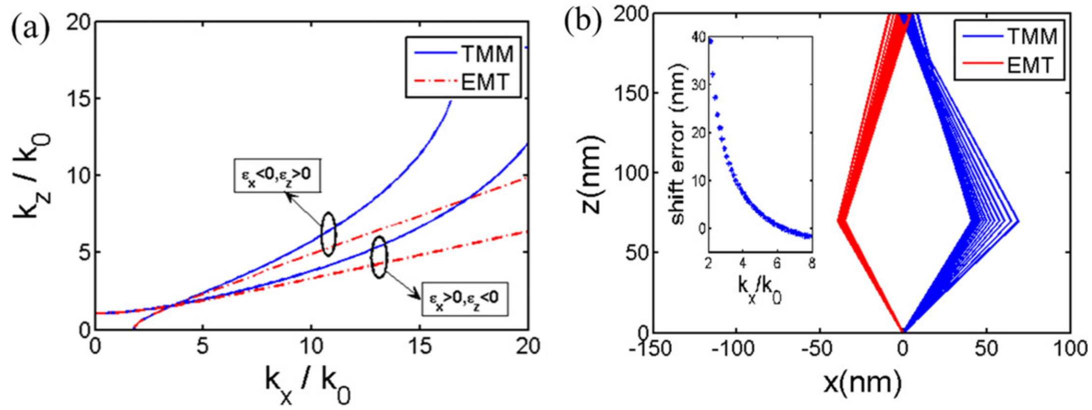

Figure 4. (*a*) Dispersion curves in the first quadrant for a fixed frequency calculated by EMT and TMM with the same parameters. (*b*) Ray trace in the imaging structure, estimated using EMT and TMM, the inner plot shows the different shift errors corresponding to different k_x.

area is enclosed by perfectly matched layers to eliminate any reflection back into the structure, thus preventing interference.

The simulation results are shown in figure 3(*a*). Light energy is transmitted symmetrically along two directions, changing its propagating direction at the interface of ML1 and ML2; the result is a focused image at the top surface of ML2. The image spot has a full-width at half-maximum (FWHM) of about 25 nm, illustrating super-resolution imaging capability. Moreover, two closely positioned objects can be clearly resolved. Figure 3(*b*) illustrates a plot of the spatial distribution of two slit objects with a centre-to-centre distance of 40 nm (black) and the corresponding images at the image plane (red). The resolving power is about 1/9 of the working wavelength (365 nm). The background associated with the image in figure 3(*b*) is believed to arise from the low k_x components, which do not follow the principal directional route in the structure, but decay exponentially and propagate in the direction normal to ML1 and ML2.

We use the TMM, which is based on a rigorous coupled wave analysis, to investigate the imaging structure designed by EMT. Figure 4(*a*) represents the dispersion curves for the presented imaging structure with EMT and TMM. The curves obtained by the two methods agree well for small k_x, but differ significantly with increasing transverse wave vector. An intuitive view of the imaging behaviour is shown in figure 4(*b*), which shows the energy flow direction for a variety of k_x, through the ray-tracing method within the multi-lens structure. Clearly, the light does not converge to one ideal image point; rather, it converges to a region extended along both transverse and normal directions, indicating some aberration in the lens. The inset of figure 4(*b*) shows the transverse shift of the converging image at a distance of 200 nm from the object. Note that low-k vectors cannot be transmitted effectively in this structure because of the band gap shown in figure 2(*a*). As seen from figure 4(*b*), a resolution of ∼20 nm can be achieved, which is consistent with the results shown in figure 3. As the film thickness increases, the extension of the focal region will be more obvious and the resolving power of the system will be reduced.

The film thickness is yet another factor influencing imaging quality that should be taken into account. Here we assume that the total number of layers in the two structures is fixed. Further simulation results (figure 5) with thicker films show reduced imaging quality using the same object and mask. This phenomenon can be explained by the fact that the increased thickness of the layers diminishes the transmission of evanescent waves, essentially through the coupling of surface plasmon modes in metallodielectric films due to the layers' resemblance to surface plasmon waveguides [50–52]. The plasmon coupling length increases as the layer thickness increases, so a broadening of the image point will be observed clearly in figures 5(*b*) and (*c*). The coupling of the propagating light to surface plasmons will be investigated in future work; here we will only analyse the imaging process employing the TMM. With the increase in film thickness, the dispersion curves calculated by the TMM are no longer hyperbolic, but rather show an exponential response with normalized k_z. The dispersion curves increase significantly within a small range of the normalized k_x, and result in a divergence of the energy flow, illustrated in figure 4(*b*).

According to figure 4(*a*), both diverging angle and converging angle increase as the film thickness increases. Thus, the expansion of the focal region can be accounted for by changing the ratio d1/d2 according to the ray-tracing analysis. Increasing the ML2 one unit cell (one pair of metal and dielectric layer) thickness while decreasing the ML1 one unit cell thickness results in a much smaller focal region, as shown in figure 5(*d*). Even if the thickness of each layer is increased up to 20 nm, super-resolution can still be achieved with a little adjustment of the theoretical triangular relation. However, it can be seen from figure 5 that the intensity has significantly decreased with the increment in film thickness. Another paradoxical factor is the absorption loss in metal films, which usually has a negative influence on imaging resolution; this effect has already been seen in the superlens. Large absorption also leads to reduced performance and resolution when transferring the large k_x component. On the other hand, slight absorption helps in eliminating the potential adverse effects of multiple reflections and refractions at the interface of two different structures.

Other than super-resolution, our lens system has the advantage of lower transmission loss when compared with similar designs, such as the hyperlens. Figure 6 plots the cross section cut from the centre of the slit for both our lens

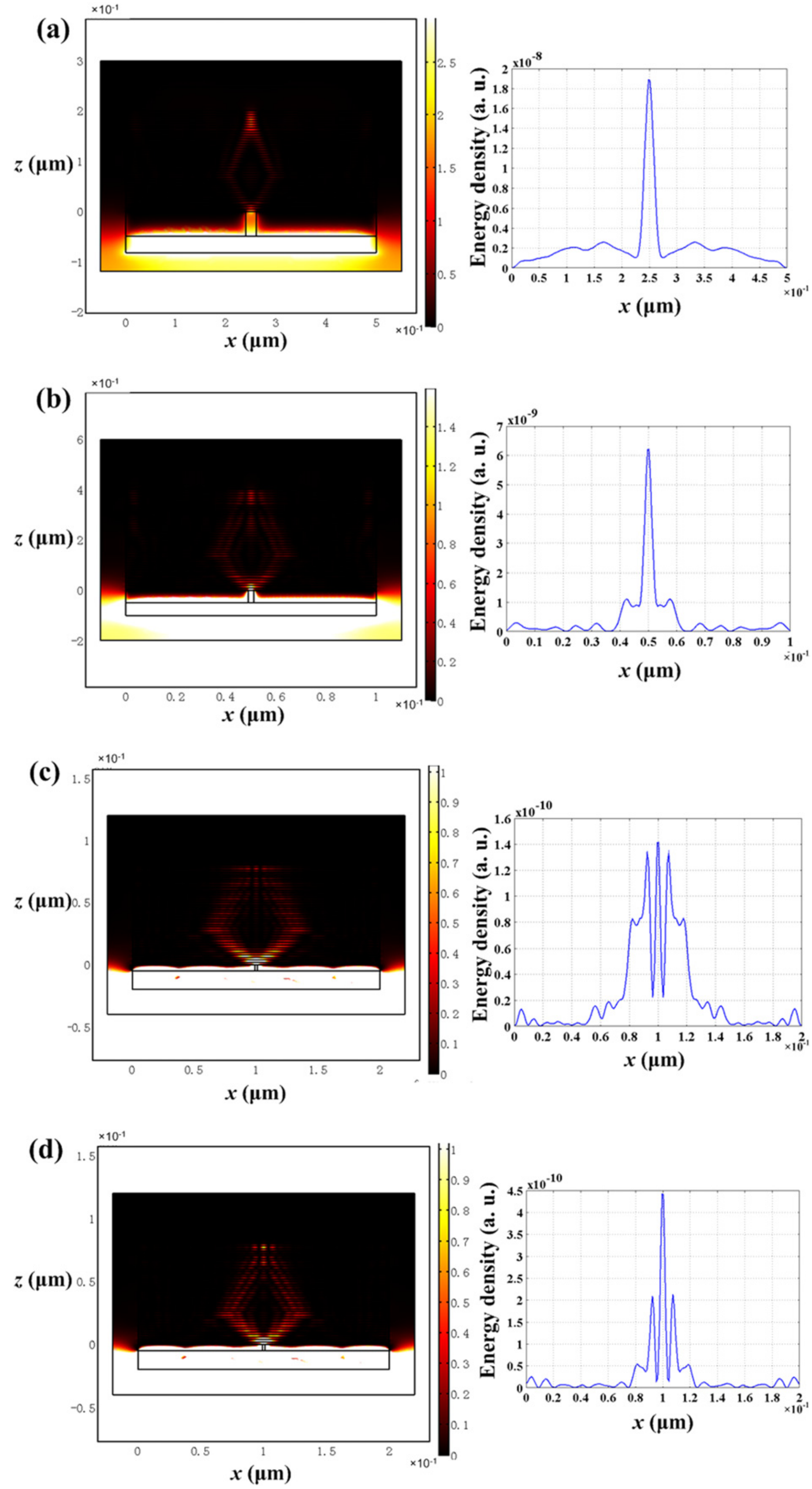

Figure 5. (*a*) Focus with FWHM of 25 nm is achieved when the thickness is 5 nm for each layer and the total thickness of the imaging structure is 200 nm. (*b*) FWHM is ∼35 nm when the layer thickness is increased to 10 nm and the total thickness of the structure is 400 nm. (*c*) FWHM is ∼400 nm when the thickness of each film is 20 nm and the total thickness of the structure is 800 nm. (*d*) Using the same structure in figure 5(*c*) while changing the thickness ratio of ML1 and ML2 based on the ray trace analysis. The size of the focus reduced back to 40 nm.

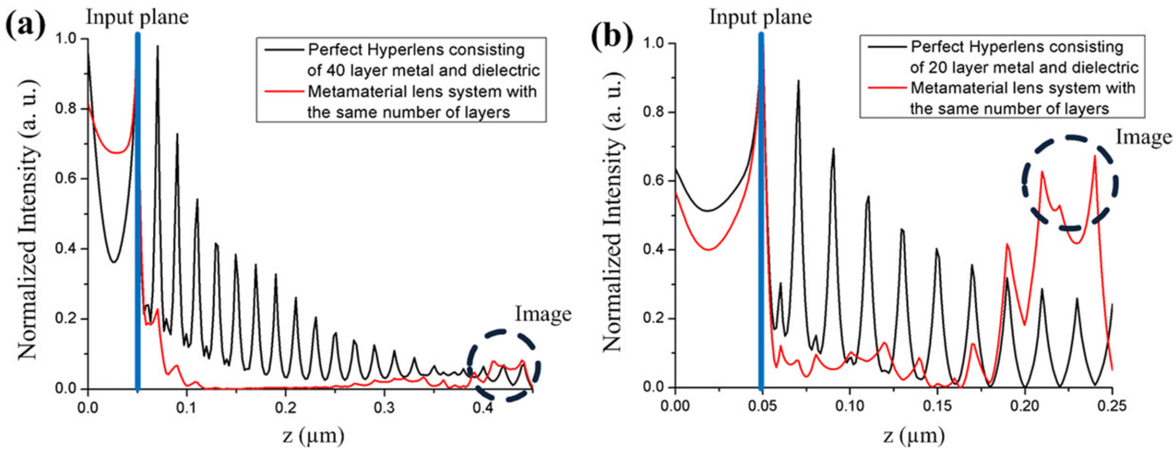

Figure 6. (*a*) Comparison of our lens system with a hyperlens configuration under the perfect matching condition ($\mathrm{Re}(\varepsilon_m) = -\varepsilon_d$). Comparable transmission (around 10%) can be observed in both systems. (*b*) Much higher transmission (50%) can be achieved in our lens system (30%) when the system is redesigned with fewer layers. All the results are obtained through a cross section cut from the centre of slit through the centre of the lens.

system and a hyperlens system with the same number of layers and the same film thickness. Here we use the same metal (silver) in both cases to avoid the external loss caused by the metal itself, as metal is the major cause of propagation loss. For the demonstrated case in figure 6(*a*), we can see that a comparable transmission efficiency is achieved by our lens system when compared with a hyperlens configuration with perfect match ($\mathrm{Re}(\varepsilon_m) = -\varepsilon_d$). Almost no transmission can be observed from $z = 100$ nm to $z = 300$ nm, confirming our claim that the image is obtained through focusing rather than direct transmission of the input light. The transmission loss can be further reduced by designing a lens system with fewer layers, as plotted in figure 6(*b*). By cutting the number of layers in half, much higher transmission efficiency can be achieved in our lens system than the hyperlens. Around 50% of incident energy is focused to the image point due to the directed transmission of almost all the large wave vector components in our metamaterial lenses system.

The metamaterial lens based super-resolution imaging structure proposed in this paper can be fabricated by confining the imaging structure and process to a planar space on a substrate. Moreover, by using e-beam lithography, it is convenient to obtain the proposed heterometallodielectric structure with the desired thickness and number of thin layers. Similar methods have also been used to demonstrate the imaging of a hyperlens on a substrate in the visible frequency range [53]. This metamaterial lens can also be integrated with optofluidic components [54–60] and can be applied in lab-on-a-chip systems [61–69].

In conclusion, we have numerically demonstrated that super-resolution imaging can be realized in a heterometamaterial structure consisting of two cascaded interlayered structures comprised of alternating dielectric and metal films. Using the EMT and TMM methods, we show that imaging with resolution nine times smaller than the light wavelength can be achieved by combining two lenses made of interlayered structures forming the metamaterial lens structure. We also show that the imaging effect can be further optimized by changing the thickness of the lens for the unit cell with different thicknesses. With its high resolution and simple structure, the proposed imaging system can be valuable for applications such as nanolithography, optical storage and bio-sensing.

Acknowledgments

The authors gratefully acknowledge the financial support from the Air Force Office of Scientific Research (AFOSR), National Science Foundation (NSF) and the Penn State Center for Nanoscale Science (MRSEC).

References

[1] Born M and Wolf E 1999 *Principles of Optics* (Cambridge: Cambridge University Press)
[2] Pendry J 2000 *Phys. Rev. Lett.* **85** 3966
[3] Shelby R A, Smith D R and Schultz S 2001 *Science* **292** 77
[4] Kwon D, Werner D H, Kildishev A V and Shalaev V M 2007 *Opt. Express* **15** 1647
[5] Yao J, Liu Z, Liu Y, Wang Y, Sun C, Bartal G, Stacy A and Zhang X 2008 *Science* **321** 930
[6] Valentine J, Zhang S, Zentgraf T, Ulin-Avila E, Genov D A, Bartal G and Zhang X 2008 *Nature* **455** 376
[7] Waele R, Burgos S P, Atwater H A and Polman A 2010 *Opt. Express* **18** 12770
[8] Burgos S P, Waele R, Polman A and Atwater H A 2010 *Nature Mater.* **9** 407
[9] Pendry J B and Ramakrishna S A 2003 *Physica* B **338** 329
[10] Melville D and Blaikie R 2005 *Opt. Express* **13** 2127
[11] Melville D O S and Blaikie R J 2006 *J. Opt. Soc. Am.* B **23** 461
[12] Podolskiy V A and Narimanov E E 2005 *Opt. Lett.* **30** 75
[13] Fang N, Lee H, Sun C and Zhang X 2005 *Science* **308** 534
[14] Lee H, Xiong Y, Fang N, Srituravanich W, Durant S, Ambati M, Sun C and Zhang X 2005 *New J. Phys.* **7** 255
[15] Pendry J B, Schurig D and Smith D R 2006 *Science* **312** 1780
[16] Wang W, Xing H, Fang L, Liu Y, Ma J, Lin L, Wang C and Luo X 2008 *Opt. Express* **16** 21142
[17] Leonhardt U 2006 *Science* **312** 1777
[18] Valentine J, Li J, Zentgraf T, Bartal G and Zhang X 2009 *Nature Mater.* **8** 568

[19] Ergin T, Stenger N, Brenner P, Pendry J B and Wegener M 2010 *Science* **328** 337
[20] Cai W, Chettiar U K, Kildishev A V and Shalaev V M 2007 *OSA Technical Digest* (CD) (Optical Society of America) paper TuD2
[21] Kwon D and Werner D H 2008 *Appl. Phys. Lett.* **92** 013505
[22] Kwon D and Werner D H 2008 *Appl. Phys. Lett.* **92** 113502
[23] Liu N, Mesch M, Weiss T, Hentschel M and Giessen H 2010 *Nano Lett.* **10** 2342
[24] Kravets V G, Schedin F and Grigorenko A N 2008 *Phys. Rev.* B **78** 205405
[25] Yang J, Huang M, Yang C, Xiao Z and Peng J 2009 *Opt. Express* **17** 19656
[26] Lin L, Wang W, Du C and Luo X 2008 *Opt. Express* **16** 6809
[27] Lin L, Wang W, Cui J, Du C and Luo X 2008 *Opt. Express* **16** 6815
[28] Liu Z, Lee H, Xiong Y, Sun C and Zhang X 2007 *Science* **315** 1686
[29] Lee H, Liu Z, Xiong Y, Sun C and Zhang X 2007 *Opt. Express* **15** 15886
[30] Zhao Y, Gan D, Cui J, Wang C, Du C and Luo X 2008 *Opt. Express* **16** 5697
[31] Xiong Y, Liu Z, Sun C and Zhang X 2007 *Nano Lett.* **7** 3360
[32] Pavel A B and Hao Y 2006 *Phys. Rev.* B **73** 113110
[33] Pavel A B, Zhao Y, Sudhakaran, Alomainy and Hao Y 2006 *Appl. Phys. Lett.* **89** 262109
[34] Zhao Y, Pavel A B and Hao Y 2006 *Opt. Express* **14** 5154
[35] Pavel A B, Zhao Y, Tse S, Ikonen P, Silveirinha M G, Simovski C R, Tretyakov S, Hao Y and Parini C 2008 *Phys. Rev.* B **77** 193108
[36] Schurig D and Smith D R 2005 *New J. Phys.* **7** 162
[37] Sihvola A 1999 *Electromagnetic Mixing Formulas and Applications* (London: Institute of Electrical Engineers)
[38] COMSOL Multiphysics, licensed to Penn State University, http://www.comsol.com/
[39] Baxter R J 1982 *Exactly Solved Models in Statistical Mechanics* (New York: Academic)
[40] Moharam M G, Grann E B, Pommet D A and Gaylord T K 1995 *J. Opt. Soc. Am.* A **12** 1068
[41] Xu T, Zhao Y, Ma J, Wang C, Cui J, Du C and Luo X 2008 *Opt. Express* **16** 13579
[42] Liu Y J, Shi J, Zhang F, Liang H, Xu J, Lakhtakia A, Fonash S J and Huang T J 2011 *Sensors and Actuators* B **156** 593
[43] Zhao Y, Lin S S, Nawaz A A Kiraly B, Hao Q, Liu Y and Huang T J 2010 *Opt. Express* **18** 23458
[44] Liu Y J, Zheng Y B, Liou J, Chiang I, Khoo I C and Huang T J 2011 *J. Phys. Chem.* C **115** 7717
[45] Hao Q, Zhao Y, Juluri B K, Kiraly B, Liou J, Khoo I C and Huang T J 2011 *J. Appl. Phys.* **109** 084340
[46] Kong J A 2005 *Electromagnetic Wave Theory* (Cambridge, MA: EMW Publishing)
[47] Smith D R and Schurig D 2003 *Phys. Rev. Lett.* **90** 077405
[48] Wood B, Pendry J B and Tsai D P 2006 *Phys. Rev.* B **74** 115116
[49] Palik E D 1985 *Handbook of optical constants of solids* (London: Academy Press)
[50] Berini P 2006 *Opt. Express* **14** 13030
[51] Buckley R and Berini P 2007 *Opt. Express* **15** 12174
[52] Berini P 2009 *Adv. Opt. Photon.* **1** 484
[53] Smolyaninov I I, Hung Y and Davis C C 2007 *Science* **315** 1699
[54] Psaltis D, Quake S R and Yang C 2006 *Nature* **442** 381
[55] Lapsley M I, Chiang I, Zheng Y B, Ding X, Mao X and Huang T J 2011 *Lab Chip* **11** 1795
[56] Huang H, Mao X, Lin S S, Kiraly B, Huang Y and Huang T J 2010 *Lab Chip* **10** 2387
[57] Lapsley M I, Lin S S, Mao X and Huang T J 2009 *Appl. Phys. Lett.* **95** 083507
[58] Mao X, Lin S S, Lapsley M I, Shi J, Juluri B K and Huang T J 2009 *Lab Chip* **9** 2050
[59] Mao X, Lin S S, Dong C and Huang T J 2009 *Lab Chip* **9** 1583
[60] Mao X, Waldeisen J R, Juluri B K and Huang T J 2007 *Lab Chip* **7** 1303
[61] Shi J, Yazdi S, Lin S S, Ding X, Chiang I, Sharp K and Huang T J 2011 *Lab Chip* **11** 2319
[62] Shi J, Huang H, Stratton Z, Lawit A, Huang Y and Huang T J 2009 *Lab Chip* **9** 3354
[63] Ahmed D, Mao X, Juluri B K and Huang T J 2009 *Microfluidics and Nanofluidics* **7** 727
[64] Shi J, Ahmed D, Mao X, Lin S S and Huang T J 2009 *Lab Chip* **9** 2890
[65] Ahmed D, Mao X, Shi J, Juluri B K and Huang T J 2009 *Lab Chip* **9** 2738
[66] Mao X, Waldeisen J R and Huang T J 2007 *Lab Chip* **7** 1260
[67] Hsiao V K S, Waldeisen J R, Zheng Y, Lloyd P F, Bunning T J and Huang T J 2007 *J. Mater. Chem.* **17** 4896
[68] Huang T J, Liu M, Knight L D, Grody W W, Miller J F and Ho C 2002 *Nucleic Acids Res.* **30** e55
[69] Shi J, Mao X, Ahmed D, Colletti A and Huang T J 2008 *Lab Chip* **8** 221